Sedimentological and geophysical properties of a ca. 4000 year old tsunami deposit in southern Spain

Article *in* Sedimentary Geology · December 2014

DOI: 10.1016/j.sedgeo.2014.09.006

CITATIONS
39

READS
1,159

2 authors:

Benjamin Koster
ROSEN Technology & Research Center GmbH
21 PUBLICATIONS **305** CITATIONS
SEE PROFILE

Klaus R. Reicherter
RWTH Aachen University
385 PUBLICATIONS **3,893** CITATIONS
SEE PROFILE

Sedimentary Geology 314 (2014) 1–16

Contents lists available at ScienceDirect

Sedimentary Geology

journal homepage: www.elsevier.com/locate/sedgeo

Sedimentological and geophysical properties of a ca. 4000 year old tsunami deposit in southern Spain

Benjamin Koster *, Klaus Reicherter

Institute of Neotectonics and Natural Hazards, RWTH Aachen University, Lochnerstr. 4-20, 52056 Aachen, Germany

ARTICLE INFO

Article history:
Received 10 June 2014
Received in revised form 22 September 2014
Accepted 24 September 2014
Available online 5 October 2014

Editor: J. Knight

Keywords:
Tsunami backwash deposits
Sedimentology
Magnetic susceptibility
Tsunami dating
3D GPR

ABSTRACT

The coastlines around the Gulf of Cádiz were affected by numerous tsunami events damaging infrastructure and causing countless human losses. A tsunami deposit at Barbate–Zahara de los Atunes, Spain, is located at various heights above mean sea level and shows several characteristics indicative of high-energy event deposition. This study uses sedimentology, foraminifera assemblage, magnetic susceptibility, X-ray fluorescence analysis, ground penetrating radar (GPR) to support an interpretation of high-energy deposition and determine the deposit's transport mechanisms and sediment source. Radiocarbon and optically stimulated luminescence dating of the tsunami deposit reveals ages of ~4000 BP and does not support the AD 1755 Lisbon event as suggested in former publications.

1. Introduction

A tsunami is an infrequent but high magnitude extreme event that, under certain circumstances, can destroy coastal infrastructure and deposit diagnostic sediments. Studying the distribution and characteristics of (pre-) historical and more recent tsunami deposits improves the accuracy of tsunami hazard maps, and therefore can help protect humans and infrastructure along coastlines all over the world.

Several geological hazards endanger the Gulf of Cádiz and the Strait of Gibraltar, related to sedimentary, tectonic and oceanographic processes (e.g., Baraza et al., 1999; Baptista and Miranda, 2009; Mulder et al., 2009; Álvarez-Gomez et al., 2011), all of which are capable of generating tsunami waves. Tsunamis can be triggered by huge submarine slumps, which can occur due to the complex hydrodynamical setting and result in further erosional characteristics. However, tsunami events in the Gulf of Cádiz are mainly triggered by major earthquakes occurring in several seismogenic fault and source zones (e.g., Gjevik et al., 1997; Baptista and Miranda, 2009; Birkmann et al., 2010; Matias et al., 2013) stretching from the Azores in the west to the Gulf of Gibraltar in the east (Mendes-Victor et al., 2009; Matias et al., 2013).

The seismicity of the region is the most studied hazard because it produces tsunamis with the largest impacts (Gràcia et al., 2010; Álvarez-Gomez et al., 2011; Baptista et al., 2011; Lario et al., 2011). Tsunamis can affect a wide area when triggered near the Gulf of Cádiz; not only were the coasts of Portugal, Spain and Morocco affected by the devastating AD 1755 Lisbon tsunami (e.g., Luque et al., 2002; Baptista and Miranda, 2009; Kaabouben et al., 2009), but also parts of the Atlantic archipelagos of Madeira, Azores and Canaries as well (e.g., Bryant, 2008; Baptista and Miranda, 2009).

Matias et al. (2013) described and analysed several active fault structures in the Gulf of Cádiz in order to produce a generation model for strong tsunamis such as of AD 1755. The authors state that combined activity of active faults in the Gulf of Cádiz region results in major earthquake recurrence periods of around 700 years for M_w 8.0 events and of 3500 years for M_w 8.7 events.

Gjevik et al. (1997) and Baptista et al. (1998) both state that the AD 1755 event originated on the continental shelf with an epicentre located between the Gorringe Bank and the Iberian coast. However, Gutscher et al. (2006, 2009) identified a subduction plane underlying an accretionary wedge, which may be able to generate M_w >8.6 earthquakes.

Within the Gulf of Cádiz numerous large tsunami events have been reported which left deposits along the Spanish and Portuguese coast during the Holocene. These events were evidenced by means of geoscientific surveys (e.g., Dawson et al., 1995; Hindson et al., 1996; Gutscher et al., 2002; Gracia et al., 2006; Kortekaas and Dawson, 2007; Lario et al., 2011), historical written reports (e.g., Baptista and Miranda, 2009; Kaabouben et al., 2009) as well as based upon numerical modelling (e.g., Gjevik et al., 1997; Baptista et al., 1998; Gutscher et al., 2006).

Previously, sedimentary evidence for at least one palaeotsunami within shallow percussion drill cores in the nearby lagoons and marshlands and at several outcrops along a beach cliff at the Gulf of

* Corresponding author.
E-mail address: b.koster@nug.rwth-aachen.de (B. Koster).

http://dx.doi.org/10.1016/j.sedgeo.2014.09.006
0037-0738/

Cádiz was found (Reicherter et al., 2010). This present study reports the results of sedimentary analyses of several outcrops along the beach cliff, reference samples from the modern beach and the marshlands (Marismas of Barbate), and shallow percussion drill cores in the nearby lagoons and marshlands. The drill core analyses complement the outcrop evidence and together prove the occurrence of ancient tsunami landfall in this region. Fresh cleaned outcrops and several new features were documented and innovative techniques in tsunami research such as spatial magnetic susceptibility (MS) measurements were undertaken to produce a two-dimensional MS surface of the deposit. Ground penetrating radar (GPR) profiles were carried out in order to reconstruct the possible palaeo-extent of the tsunami deposits (cf., Koster et al., 2014). Additionally, a high resolution GPR antenna for scanning of outcrop walls was used in order to detect further sediment characteristics and to combine the results with the magnetic susceptibility measurements. Lastly, dating results from the tsunami deposits using both radiocarbon and optically stimulated luminescence (OSL) dating techniques are presented.

2. The Gulf of Cádiz — study area and tsunami history

The Gulf of Cádiz is located west of the Mediterranean Sea adjacent to the Strait of Gibraltar (Fig. 1). It is enclosed by the Iberian Peninsula to the north and the African continent to the south, while to the west it is open to the Atlantic Ocean. The arc-shaped northern margin is generally dominated by coastal lowlands following a general northwest–southeast alignment. The study area is located at the southeastern part of the Gulf of Cádiz, at a beach between the cities of Barbate and Zahara de los Atunes in the Gulf of Cádiz (Fig. 1A, B). The study area connects to the edge of the Cape Trafalgar region in the northwest where Whelan and Kelletat (2005) state that boulder deposits provide possible evidence of the AD 1755 Lisbon tsunami.

The coast of the study area is dominated by a rocky cliff which is 0.7–5.0 m high. The investigated tsunami deposit can be found within the retreating erosive cliff at 1.8–5.0 m above mean sea level. The deposit also has a variable sedimentary composition (Reicherter et al., 2010). A dark brown coloured layer of gravel, sand and silt, shows a fining upward sequence with a palaeoflow direction towards the sea. This is due to imbricated clasts, which rest directly on the folded Betic substratum of Cretaceous to Eocene deposits (Grützner et al., 2012).

The list of historically documented, recorded and sedimentary evidenced tsunami deposits along the Gulf of Cádiz in Portugal, Spain and Morocco includes ~37 tsunami events (e.g., Soloviev, 1990; Luque et al., 2001, 2002; Ruiz et al., 2005, 2008, 2013; Morales et al., 2008; Baptista and Miranda, 2009; Kaabouben et al., 2009; Gràcia et al., 2010; Lario et al., 2011; Rodríguez-Vidal et al., 2011a,2011b). The number of Holocene tsunami deposits along the coast of the Gulf of Cádiz for which sedimentary evidence exists is at least at 22. There are only five events for which historically documented records can be matched with corresponding coeval tsunami deposits. All others were solely reported by historical documents or tide measurements.

3. Methods

3.1. Sedimentological analysis on outcrops and auger drilling

Surface sampling (55 samples; compare Table 1) from the cleaned outcrops at the cliff as well as several drillings with an auger drilling unit were carried out. The latter was mainly used to verify the ground penetrating radar wave depths and layer boundaries. Wet sieving was undertaken for sandy and coarser samples, and laser diffraction analysis for samples dominated by silt and clay fractions. The Retsch AS 200 basic sieving machine was used for wet sieving. For grain sizes below 2.0 mm a Beckmann Coulter LS 13320 laser diffraction particle size analyser was used with a detection range between 0.04–2000 µm. The samples were pre-treated with 10% hydrogen peroxide (H_2O_2) for 24 hours for sediment disaggregation before particle size analyses.

Statistical parameters were calculated after Blott and Pye (2001) from the results of grain size distribution. In this study sorting versus mean-, sorting versus median- and CM diagrams were used to draw conclusions on the depositional environment of the tsunami deposits.

3.2. Micropalaeontological analysis

The samples for micropalaeontological analysis (20 samples) were all from the inferred sandy tsunami deposit (see Table 1), except for

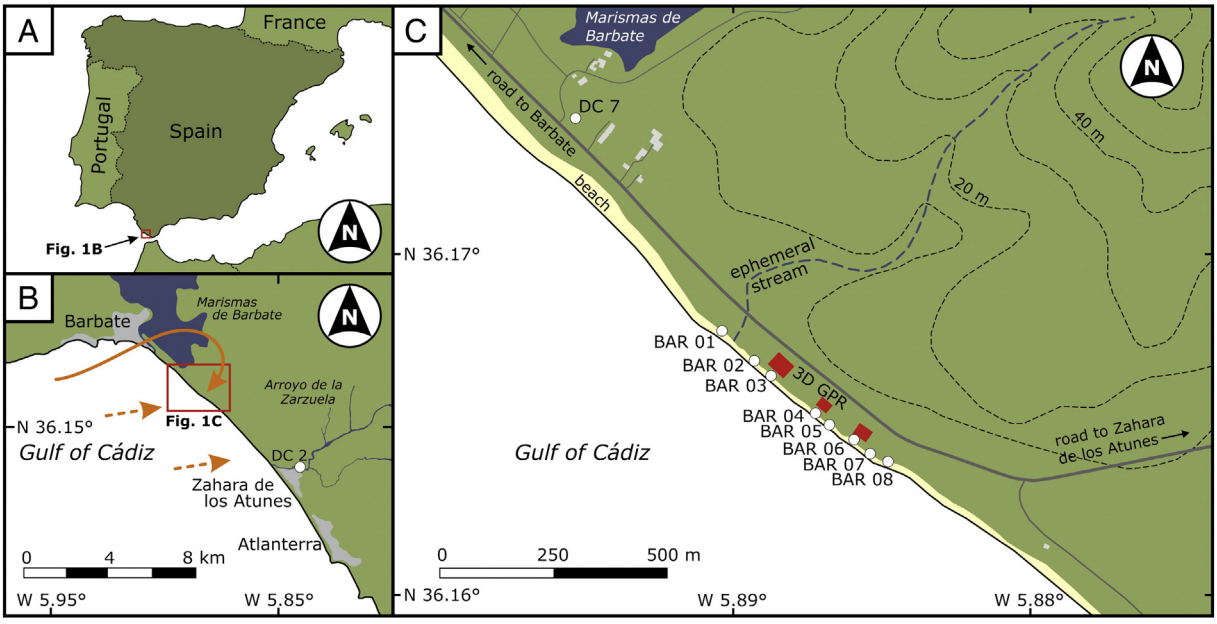

Fig. 1. (A) Overview map of the study area. (B) Location of the study area between Barbate and Zahara de los Atunes (Gulf of Cádiz) and drill core DC 2 (cf., Reicherter et al., 2010) marked with white circle near Zahara de los Atunes. Hemicycle-shaped tsunami propagation and continued tsunami landfall is marked by orange coloured arrows. (C) Detailed map of the study area; white circles illustrate investigated beach outcrops as well as drill core DC 7 from previous studies (cf., Reicherter et al., 2010), and red boxes show the locations of ground penetrating radar (GPR) grids. Grey boxes illustrate houses and buildings. (For interpretation of the references to colour in this figure legend, the reader is referred to the web version of this article.)

Table 1
Samples taken from the outcrops with sampling depth, individual type of grain size analysis (WS = wet sieving; L = laser diffraction) and foraminifera tests with results of micropalaeontology (SF = shell fragments; gastr. = gastropods; GL sp. = *Globigerina* sp.; EL cr. = *Elphidium crispum*; RA sp. = *Radiolaria* sp.; PU sp. = *Pullenia* sp.; AM bec. = *Ammonia beccarii*; TI sp. = *Ticinella* sp.; BI sp. = *Biticinella* sp.; RO sp. = *Rotalipora* sp.; HE sp. = *Heterohelix* sp.; GS sp. = *Glomospira* sp.). (CC) refers to coarse clasts where it was not possible to carry out wet sieving or laser diffraction.

sample	Type of grain size analysis	Foraminifera analysis	Micropalaeontology
BAR 01:			
0–13 cm	WS	–	
13–32 cm	L	√	SF
32–57 cm	L	–	
57–87 cm	L	–	
87–110 cm	L	–	
BAR 02:			
0–7 cm	WS	–	
7–38 cm (a) (7–18 cm)	L	√	GL sp. (rew.); SF
7–38 cm (b) (18–28 cm)	L	√	GL sp. (rew.); EL cr.; SF
7–38 cm (c) (28–38 cm)	L	√	GL sp. (rew.); SF
38–46 cm	WS	–	
46–72 cm	WS	–	
72–80 cm	L	–	
BAR 03:			
0–9 cm	WS	–	
9–30 cm	L	√	GL sp. (rew.)
30–88 cm (a) (30–60 cm)	L	√	RA sp. (rew.); GL sp.; EL cr. (rew.)
30–88 cm (b) (60–88 cm)	L	√	RA sp. (rew.); GL sp.; EL cr. (rew.)
88–105 cm	WS	–	
115–130 cm	L	–	
130–140 cm	WS	–	
140–159 cm	WS	–	
159–160 cm	(CC)	–	
BAR 04:			
0–14 cm	WS	–	
14–70 cm (a) (14–30 cm)	L	√	EL cr. (rew.)
14–70 cm (b) (30–50 cm)	L	√	EL cr. (rew.)
14–70 cm (c) (50–70 cm)	L	√	EL cr. (rew.); GL sp. (rew.)
70–91 cm	WS	–	
91–150 cm	(CC)	–	
BAR 05:			
0–40 cm	WS	–	
40–90 cm	L	√	GL (rew.); PU sp.
90–230 cm (a) (90–110 cm)	WS	–	
90–230 cm (b) (110–140 cm)	WS	–	
90–230 cm (c) (140–180 cm)	WS	–	
90–230 cm (d) (180–230 cm)	WS	–	
BAR 06:			
0–10 cm	WS	–	
10–100 cm (a) (10–40 cm)	L	√	SF
10–100 cm (b) (40–70 cm)	L	√	SF
10–100 cm (c) (70–100 cm)	L	√	SF
100–110 cm	WS	–	
110–200 cm (a) (110–120 cm)	WS	–	
110–200 cm (b) (120–160 cm)	WS	–	
110–200 cm (c) (160–200 cm)	WS	–	
BAR 07:			
0–10 cm	WS	–	
10–30 cm	WS	–	
30–110 cm	L	√	AM bec.; GL sp.; EL cr.; SF; gastr.
110–140 cm	WS	–	
140–200 cm	WS	–	
BAR 08:			
0–30 cm	WS	–	
30–40 cm	WS	√	SF
40–72 cm (a) (40–54 cm)	WS	–	
40–72 cm (b) (54–72 cm)	WS	–	
72–108 cm	WS	–	
Modern beach:			
BAR beach 01 0–30 cm	WS	√	SF; gastr.
BAR beach 02 0–30 cm	WS	√	EL cr.; SF; gastr.
Marshlands:			
BAR Marismas 01 0–30 cm	L	√	RA sp.; TI sp.; BI sp.; RO sp.; HE sp.; PR
BAR Marismas 02 0–30 cm	L	√	RA sp.; TI sp.; BI sp.; RO sp.; HE sp.; GS sp.; PR

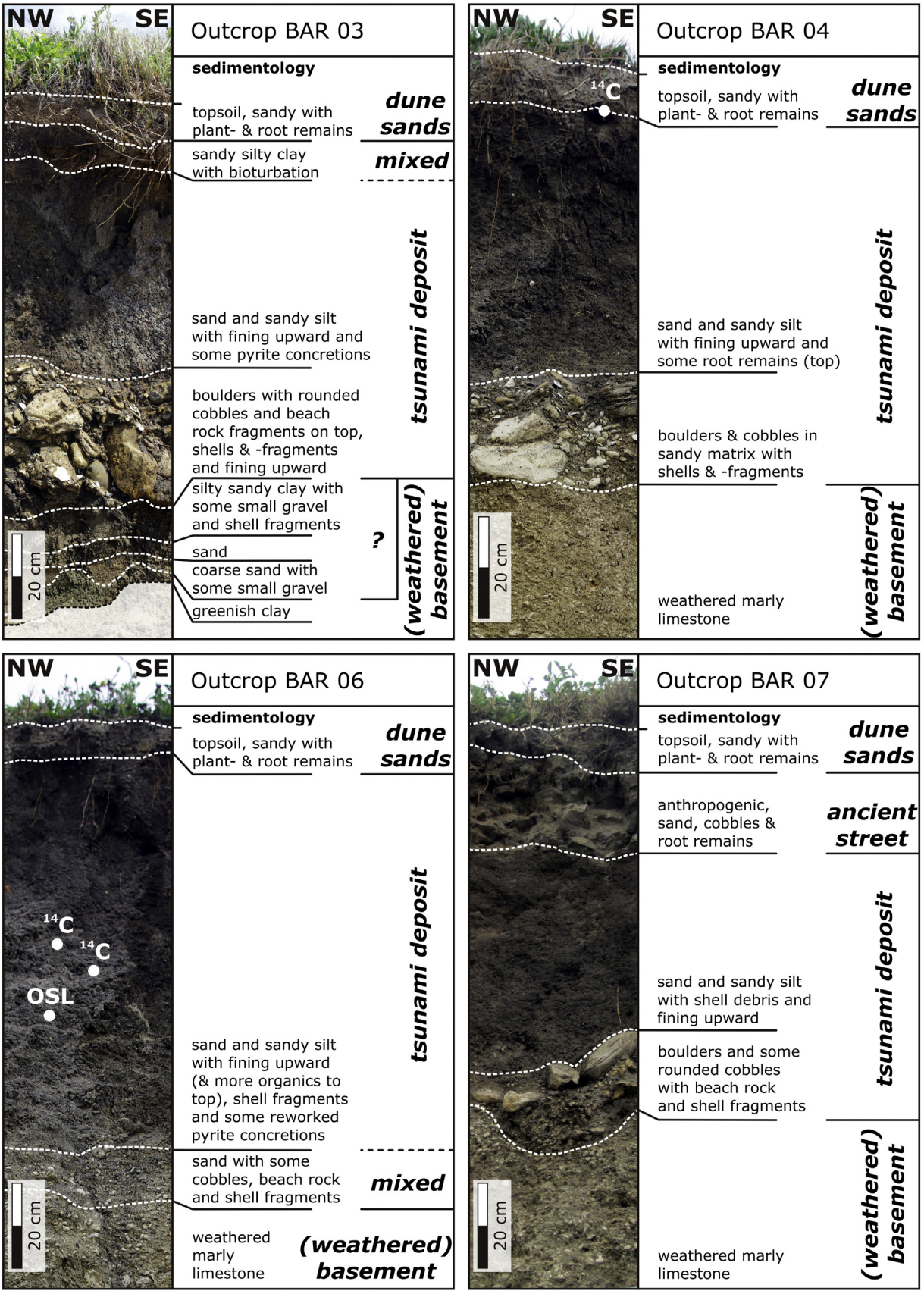

Fig. 2. Sedimentological analysis and interpretation of four outcrop examples from the study area (for location see Fig. 1C). The variable sedimentological settings regarding the tsunami deposit and the basement (weathered Cretaceous–Eocene deposits) are illustrated. The beachrocks along the cliff have an inferred age of MIS 5 (Zazo et al., 1999).

reference samples from the modern beach and adjacent marshlands. The samples were cleaned by removing sediments finer than 0.063 mm. The sieved samples were dried at 40 °C and then analysed with a Zeiss Stemi DV 4 reflecting-light microscope. The classification of Loeblich and Tappan (1988) and Murray (2008) was used as taxonomic reference. The number of foraminiferal tests within all of the samples was generally low.

3.3. Radiocarbon (^{14}C) dating

In 2009 several shells of *Acanthocardium* sp. were taken from the outcrops (e.g., BAR 06, Fig. 2) for radiocarbon dating in the Keck Carbon Cycle AMS facility at Irvine CA (USA). One sample (RC-BAR 04 (2A)) was taken close to outcrop BAR 04 from the top of the tsunami deposit below an overlying dune deposit (Fig. 2). Additionally, one sample of charcoal (RC-DC2 Zahara TL) from a layer within drill core DC 2 Zahara (location in Fig. 1B) was radiocarbon dated at GEOMAR Helmholtz Centre for Ocean research in Kiel (Germany). This radiocarbon sample from a clayey peat layer (2.58 m depth) was taken directly below a whitish sand sheet, which is interpreted as a possible tsunami deposit.

All radiocarbon dates were calibrated with OxCal 4.2 software (Bronk Ramsey, 2009) using the atmospheric "IntCal13" and marine "Marine13" calibration curves of Reimer et al. (2013); a reservoir effect of 440 years was considered (e.g., Dabrio et al., 2000).

3.4. Optically stimulated luminescence (OSL) dating

Two OSL samples of sand at outcrop BAR 06 were taken with metallic tubes (Fig. 2). Both samples were taken approximately 2 m apart from each other laterally and from the same layer. The samples have been analysed in the laboratory of the Institute of Geography at Cologne University (Germany) using measuring techniques after Murray and Wintle (2000) and a finite mixture model for equivalent dose after Galbraith and Green (1990). The OSL dating technique seems to be a credible tool for tsunami dating (e.g., Brill et al., 2012); however, this dating technique also has some limitations, e.g., the incomplete zeroing of the luminescence during the tsunami event is possible.

3.5. Magnetic susceptibility (MS) measurements

MS measurements were performed with a Bartington Instruments MS2 with MS2K sensor. The MS can be used to distinguish materials from different origins (e.g., Mullins, 1977), due to their varying content of ferromagnetic, diamagnetic or paramagnetic minerals. The MS value of a sample is given in dimensionless SI units (Dearing, 1994).

Beside MS measurements with a 2 cm spacing on all outcrops, 5 cm vertical and horizontal grid measurements were also carried out at outcrop BAR 03 and BAR 07. The grid area was cleaned and smoothed before measuring the MS to avoid errors caused by surface contamination or weathering influences. The MS grid values were processed with Surfer 11 software (Golden Software) and gridded with "natural neighbour" statistical gridding method with a resolution of 5 cm.

3.6. Geochemical analysis

At least one X-ray fluorescence (XRF) measurement was carried out in the laboratory on all bulk samples from the outcrops and additionally on all reference samples from the modern beach and the marshlands with a handheld XRF spectrometer (Niton XLt 700 series; error 11%, accuracy 97%). Some layers were sampled at three positions from base to top. XRF measurements were carried out for 60 s for each sample which were taken from the cleaned outcrop surfaces (the same as used for sedimentological analysis). The XRF spectrometer used is able to detect 18 different elements (Sb, Ag, Sr, Rb, As, Hg, Zn, Cu, Ni, Co, Fe, Mn, Cr, V, Ti, Sc, Ca and K) using a Cd-109 isotope source and a SI PIN-diode detector. Based on the results, the Ca/Fe- and the Ca/Ti-ratios are presented as the best tracers for determining different characteristics, such as the identification of marine and terrestrial sedimentary environments. The Ca/Fe-ratio and the Ca/Ti-ratio were calculated (cf., Vött et al., 2011; Chagué-Goff et al., 2012) to differentiate between marine and terrigenous components. Unfortunately, potential salinity indicators as presented by Chagué-Goff (2010) and Chagué-Goff et al. (2012) could not be tested due to the limited amount of elements detected by the XRF spectrometer.

3.7. Ground penetrating radar (GPR)

Ground penetrating radar (GPR) was used for subsurface investigations. GPR equipment during fieldwork consisted of a GSSI SIR-3000 data recording unit, 400 MHz and 900 MHz antennae, a survey wheel and handheld GPS. The topography on top of the cliff where the GPR measurements were carried out is mostly flat. Data processing was performed with ReflexW V7.0 (Sandmeier Scientific Software) and included static correction, background removal, gain adjustments and velocity adaption for time–depth conversions.

Measurements with the 400 MHz and 900 MHz GPR antenna were carried out with a trace increment of 2 cm and a sample rate of 512 samples per scan. The 900 MHz antenna has a higher resolution of ~0.5-2.0 cm but a lower penetration depth of 0.8-1.5 m. A resolution of 3-7 cm and depth of up to 4 m can be achieved with the 400 MHz GPR antenna.

The 400 MHz GPR antenna was used for scanning on top of the cliff, while the 900 MHz GPR antenna was used for scanning of the cliff walls. Data processing of the 900 MHz antenna data also includes exporting the first 2 ns (~8 cm) of each trace increment: this two way traveltime (TWT) corresponds to the penetration depth of the Bartington MS2 magnetic susceptibility sensor (5–10 cm depending on material). The results are plotted in curves, which are compared to the MS data. The GPR wave intensity values are given in dimensionless units.

3.8. Subsurface modelling

Based on the GPR data and its interpreted layer geometry, it is possible to reconstruct the raw extent of the palaeotsunami deposits in (pseudo-) 3D models. Picked layer data (of tsunami top and base) from the GPR profiles were processed with Surfer 11 software and gridded with "local polynomial" statistical gridding method. This method is based on a locally weighted least squares regression from a search ellipse at each individual node within the grid.

4. Results

4.1. Sedimentological characterisation of the outcrops

Several outcrops can be found along the 5 km long beach section between Barbate and Zahara de los Atunes. Since then winter storms have eroded the beach section and exposed new outcrops over the years.

Along the cliff is a 0.1–0.4 m thick layer containing large stones, boulders of beachrock (of MIS 5e and Pleistocene age; e.g., Zazo et al., 1999) as well as subangular to rounded sandstones of the Cretaceous/Eocene basement rock, shells (e.g., *Acanthocardia tuberculata*, *Acanthocardia aculeata*, *Glycimeris glycimeris*) and gastropods which can be observed in several outcrops (Fig. 2). Overlying this is a 0.7–1.0 m thick dark mixed sand layer (see Fig. 2). This layer contains a fining upward sequence consisting of sand at the base to silty sand at the top. The grain size distribution of the whole tsunami sequence is characterised by a trimodal distribution: the boulders at the base, the overlying sand at the base of the dark coloured sand layer, and the mostly sandy silt/silty sand deposits at the top of the tsunami deposit. The layer comprises light yellowish beach sands, a huge amount of dark coloured organic material, charcoal remains, small

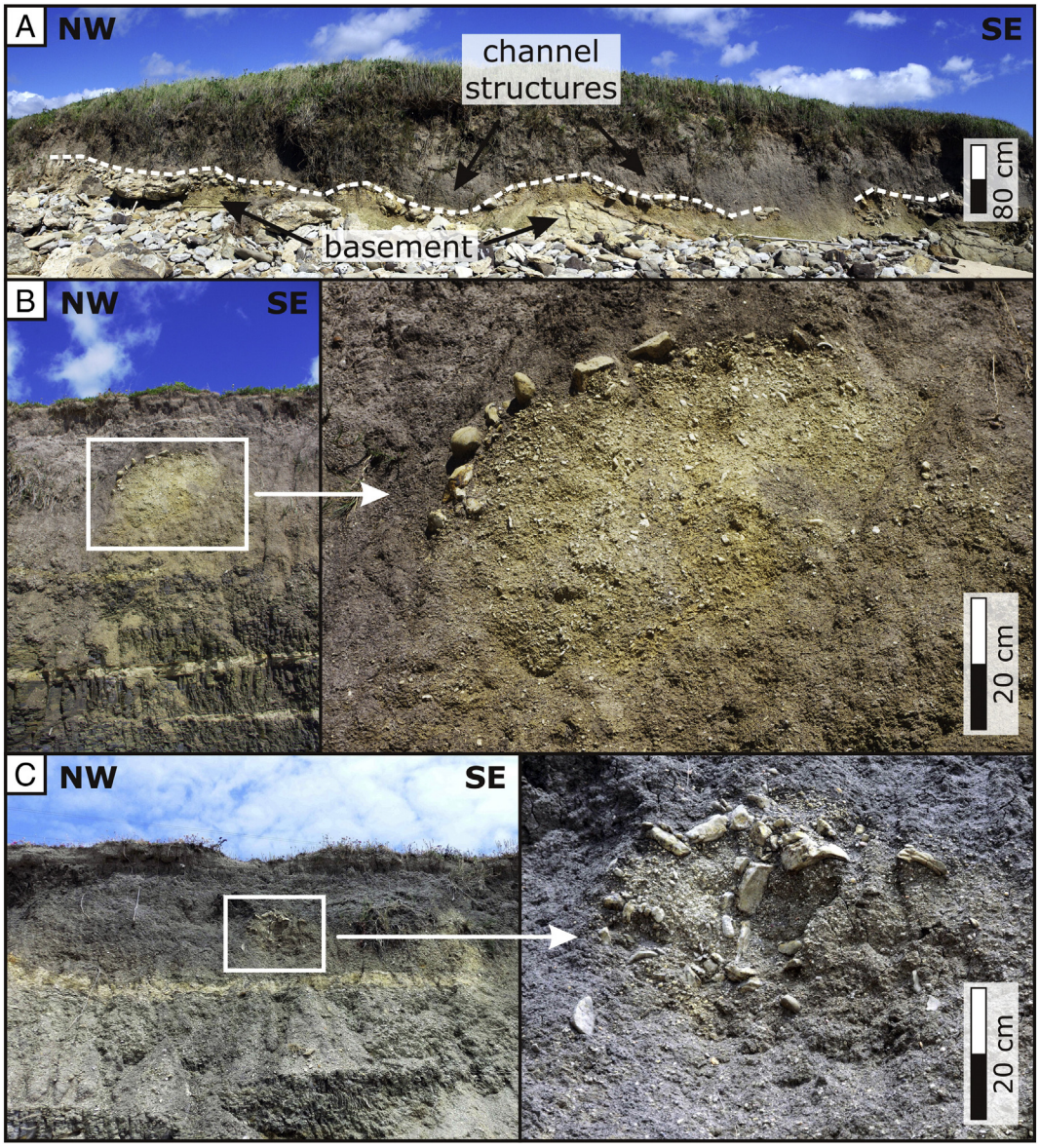

Fig. 3. Photographs of different geomorphological and sedimentary features along the beach cliff: channels (A), a clast coated mud ball (B; and detail) and two adhered clast coated mud balls inside the fine grained matrix of the tsunami deposit (C; and detail).

shells and shell fragments as well as reworked pyrite concretions from Cretaceous/Eocene rocks.

Both layers are described as a single graded tsunami backwash deposit (Reicherter et al., 2010) due to seaward imbricated clasts, channel structures (Figs. 3A, 4), a mixture of beach sands and organic material from the marshlands.

An armoured mud ball or clast-coated clay clast was found at outcrops BAR 04, BAR 05 and BAR 07 (Figs. 3B, C, 4). This ball-shaped feature contains compacted sand, clay and pieces of beachrock in the inner part, while its outside is characterised by coarser clasts and boulders (up to 30 cm). These characteristic balls are "floating" inside the sandy tsunami deposit's matrix. The diameter ranges between ~0.4 m at BAR 07 and up to ~1.2 m at BAR 05.

The deposits are relatively well sorted but at outcrop BAR 06 are the samples poorly to very poorly sorted (Fig. 4). If grain size and sorting are compared with the reference samples from the marshland and the modern beach, the samples from the tsunami layer in the cliff are intermediate between both.

Fig. 5A is a bivariate plot of phi-values of sorting versus mean grain size. The plot of samples from the tsunami deposit and the marshlands are clearly divided in their fields of low and high-energy influence (Fig. 5A). Unfortunately, some sorting values are below 1 and are not depicted in this kind of bivariate logarithmic plot. Therefore, the recent data from the beach cliff, the drill core data from Reicherter et al. (2010) (drill cores from Barbate and Tarifa) as well as the recent examples from Szczuciński et al. (2012) were applied in a metric sorting versus median plot (Fig. 5B). Most of the samples from the cliff are in the field of high-energy deposits, whereas reference samples from the marshlands are in the field of partially open to restricted estuary. The μm-values of median versus the coarsest percentile are plotted in a double logarithmic diagram (Fig. 6) to differentiate between the sediment's deposition processes.

4.2. Micropalaeontological content

The foraminiferal abundance within the modern beach samples is relatively low. Some shell debris, some gastropods as well as some *Elphidium crispum* were found but these were clearly reworked. The samples from the dark coloured sand deposit (see Table 1) do not have as much shell debris as the reference beach samples; however,

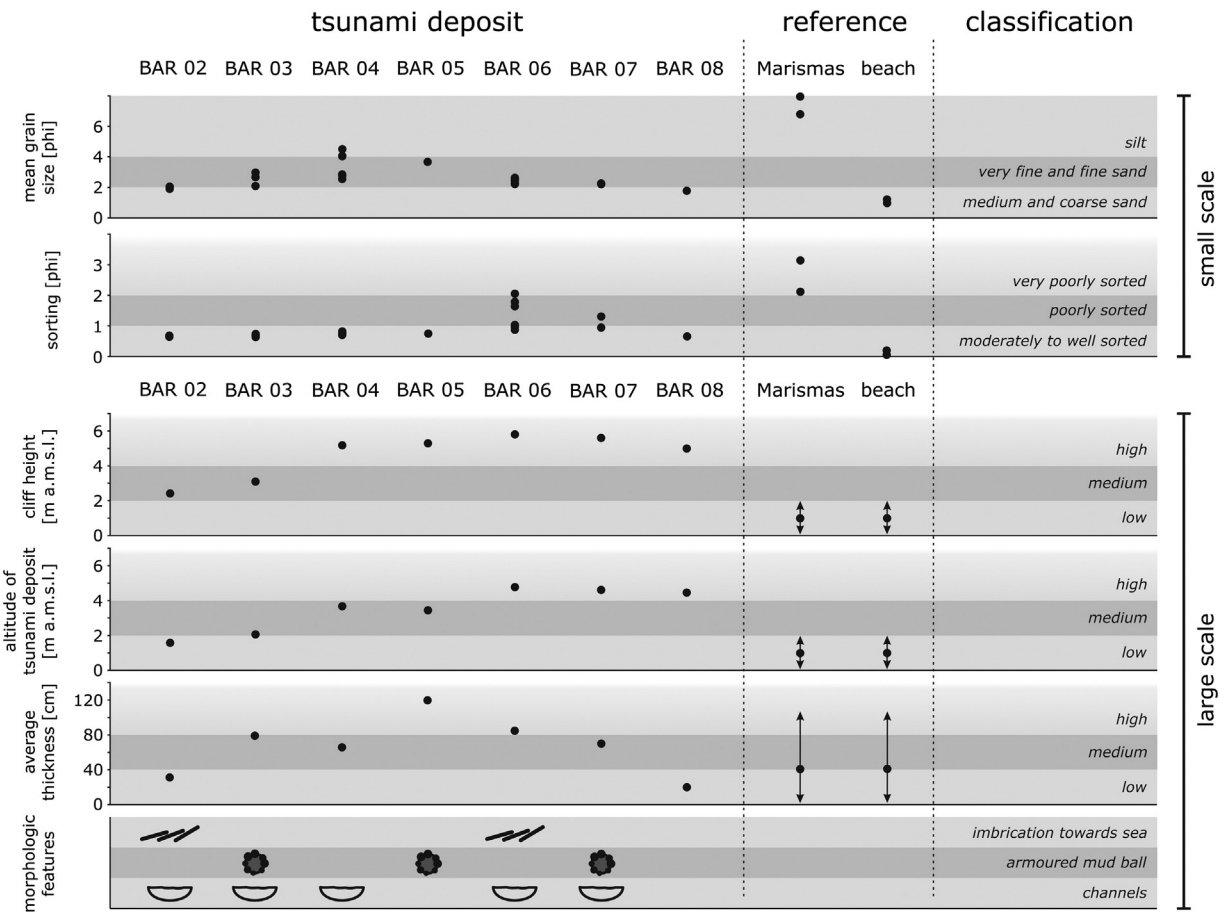

Fig. 4. Geomorphological and sedimentary features as well as grain size analysis and sorting compared to reference samples from the Marismas of Barbate (marshlands) and the recent beach sediments.

within the sampled deposits from the cliff several *Globigerina* sp., *Radiolaria* sp. and *Elphidium crispum* as well as a few gastropods were found. All of these species are common in marine to brackish-hypersaline environments (e.g., Hofrichter et al., 2003; Schiebel and Hemleben, 2005). Additionally, individual *Pullenia* sp. and *Ammonia beccarii* were found within the samples from the cliff.

The foraminiferal assemblage of the marshland reference samples has numbers of each poorly preserved and reworked species: several *Biticinella* sp., *Ticinella* sp., *Rotalipora* sp., *Heterohelix* sp., *Glomospira* sp. and some individual *Radiolaria* sp. were detected.

4.3. Tsunami dating

Radiocarbon dating from the study area resulted in calibrated ages mainly >36,600 years BP (Table 2), but sample RC-BAR 04 (2A) resulted in an age between 1260 and 1299 years BP.

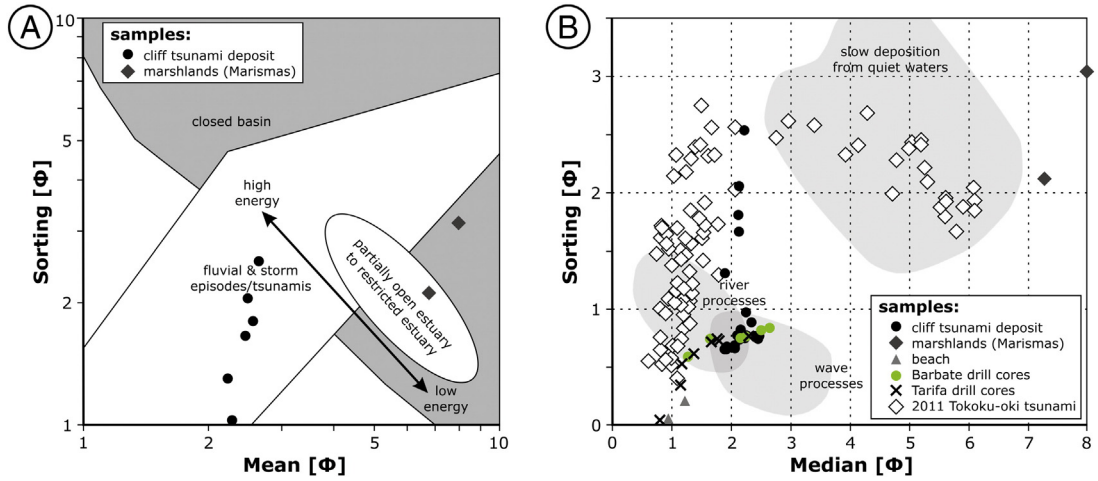

Fig. 5. (A) Bivariate logarithmic plot of sorting (phi = Φ) versus mean grain size (phi = Φ) after Lario et al. (2002) and (B) bivariate metric plot of sorting (phi = Φ) versus median grain size (phi = Φ) compared to the characteristics of the tsunami samples of the AD 2011 Tohoku-oki event (see Szczuciński et al., 2012). Plotted values from drill core samples taken in the vicinity of Tarifa are calculated using data from Reicherter et al. (2010).

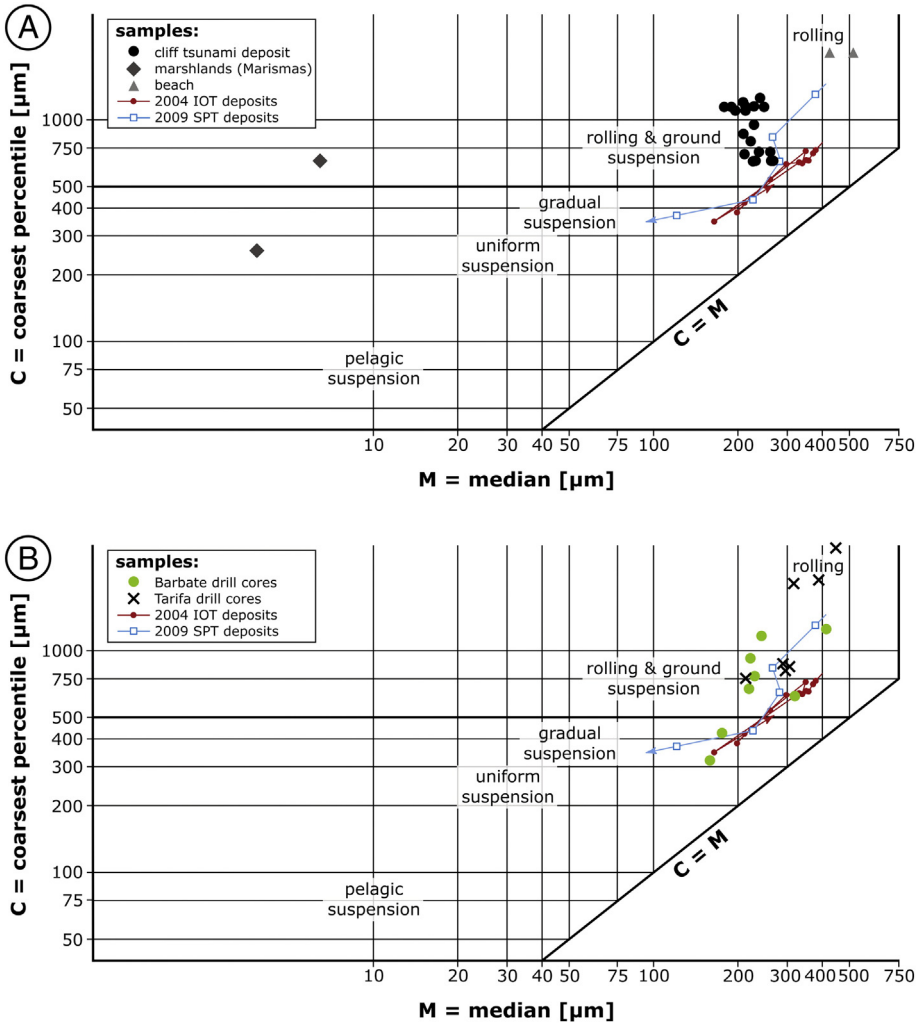

Fig. 6. (A) CM diagram of the tsunami deposit samples along the beach cliff of Barbate as well as reference samples from beach and marshland compared to the characteristics and transport mechanisms of the AD 2004 IOT (=Indian Ocean Tsunami; cf., Wassmer et al., 2010) and the AD 2009 SPT (=South Pacific Tsunami; cf., Chagué-Goff et al., 2011); (B) CM diagram of tsunami samples taken in 2008 from drill cores at Barbate and in the vicinity of Tarifa (see Reicherter et al., 2010) compared to the recent examples of the deposits of the AD 2004 IOT (=Indian Ocean Tsunami; cf., Wassmer et al., 2010) and the AD 2009 SPT (=South Pacific Tsunami; cf., Chagué-Goff et al., 2011).

The radiocarbon age data from a sample of drill core DC 2 Zahara at 2.58 m depth (cf., Reicherter et al., 2010) carried out in the tidal channel area, which is probably occasionally flooded (Moreno et al., 2010), resulted in a calibrated age between 5484 and 5587 BP (Table 2). This specific overlying potential tsunami deposit in drill core DC 2 Zahara was, therefore, deposited after 5484 BP. It is not known how much of the clayey organic-rich layer was eroded during deposition.

The OSL dating of two samples at outcrop BAR 06 gives an age of around 4000 BP for the deposits (BAR 06-1 selected: 4320 ± 900 BP and BAR 06-2 selected: 3880 ± 560 BP, Table 3). These selected dates relate to "fast component" aliquots with fast zeroing of the luminescence.

4.4. Magnetic susceptibility results

At outcrop BAR 03 three different areas can be differentiated according to their MS (see Fig. 7, left). The dimensionless MS values in the contour map vary between −2 and 24. The upper area from 0 to −0.9 m is characterised by values of 4–10 and significantly higher values at different depths. The following area (from −0.90 to −1.25 m) has values of

Table 2
Radiocarbon dating results from different shell samples (all RC-BAR samples) from the tsunami deposit along the beach cliff and a bulk sample of the tsunami deposits of drill core DC 2 (sample RC-DC2 Zahara TL) from the Zahara de los Atunes region (cf., Reicherter et al., 2010). Probably sample RC-BAR 04 (2A) has been taken at the surface of the tsunami deposit to a recent dune. A reservoir effect of 440 years is already considered in the presented data.

Sample	Lab code	conventional ^{14}C age	1 sigma calibration	2 sigma calibration	Median
RC-BAR 01 (3A)	UCIAMS-73814	35,600 ± 290 BP	39,852 to 40,564 cal BP	39,535 to 40,957 cal BP	40,219 cal BP
RC-BAR 01 (3A-1)	UCIAMS-75360	32,720 ± 180 BP	36,348 to 36,869 cal BP	36,192 to 37,387 cal BP	36,646 cal BP
RC-BAR 04 (2A)	UCIAMS-73813	1335 ± 15 BP	1275 to 1291 cal BP	1260 to 1299 cal BP	1282 cal BP
RC-BAR 06 (1A)	UCIAMS-73812	34,380 ± 250 BP	38,578 to 39,136 cal BP	38,398 to 39,519 cal BP	38,884 cal BP
RC-BAR 06 (1D)	UCIAMS-73815	41,270 ± 580 BP	44,252 to 45,293 cal BP	43,676 to 45,818 cal BP	44,765 cal BP
RC-DC2 Zahara TL	HAM-3931	4795 ± 25 BP	5580 to 5587 cal BP 5484 to 5527 cal BP	5574 to 5592 cal BP 5474 to 5549 cal BP	5512 cal BP

Table 3
Optically stimulated luminescence (OSL) dating results from 2 samples of the tsunami deposit from study area BAR 06.

Sample	Depth [m]	Number of aliquots	Aliquots [%]	Equivalent dose [Gy]	OSL age [ka]
BAR 06-1	0.7	52	4	1.90 ± 0.33	1.55 ± 0.30
			47	2.83 ± 0.33	3.92 ± 0.42
			43	7.82 ± 0.55	6.35 ± 0.68
			6	15.20 ± 1.02	12.30 ± 1.70
BAR 06-1 selected	0.7	15	100	5.32 ± 1.02	**4.32 ± 0.90**
BAR 06-2	0.7	51	2	2.39 ± 0.39	1.78 ± 0.33
			14	5.56 ± 0.51	4.16 ± 0.51
			23	8.58 ± 0.78	6.41 ± 0.79
			41	14.6 ± 1.00	10.90 ± 1.20
			20	24.80 ± 2.00	18.60 ± 2.10
BAR 06-2 selected	0.7	27	14	5.19 ± 0.61	**3.88 ± 0.56**
			32	8.28 ± 0.84	6.19 ± 0.81
			28	12.80 ± 1.60	9.60 ± 1.44
			27	20.60 ± 1.80	15.40 ± 1.90

−2 to 5. The base of the section (deeper than −1.25 m) is similar to the upper area with moderate MS values. The statistical parameters of mean and standard deviation for the whole section are 5.3 and 3 respectively. The MS values at outcrop BAR 07 are generally slightly higher than at outcrop BAR 03 (see Fig. 7, right). Characteristic values can be defined for different sedimentological deposits (compare Fig. 7, bottom right). While the sandy tsunami deposit's values range from 4–11, the base of the tsunami deposit (characterised by boulders) has values of −2 to 5.

4.5. XRF elements and ratios

The elemental composition and ratios (see Fig. 8) indicate a change of material and prove the boundaries of the tsunami deposit although

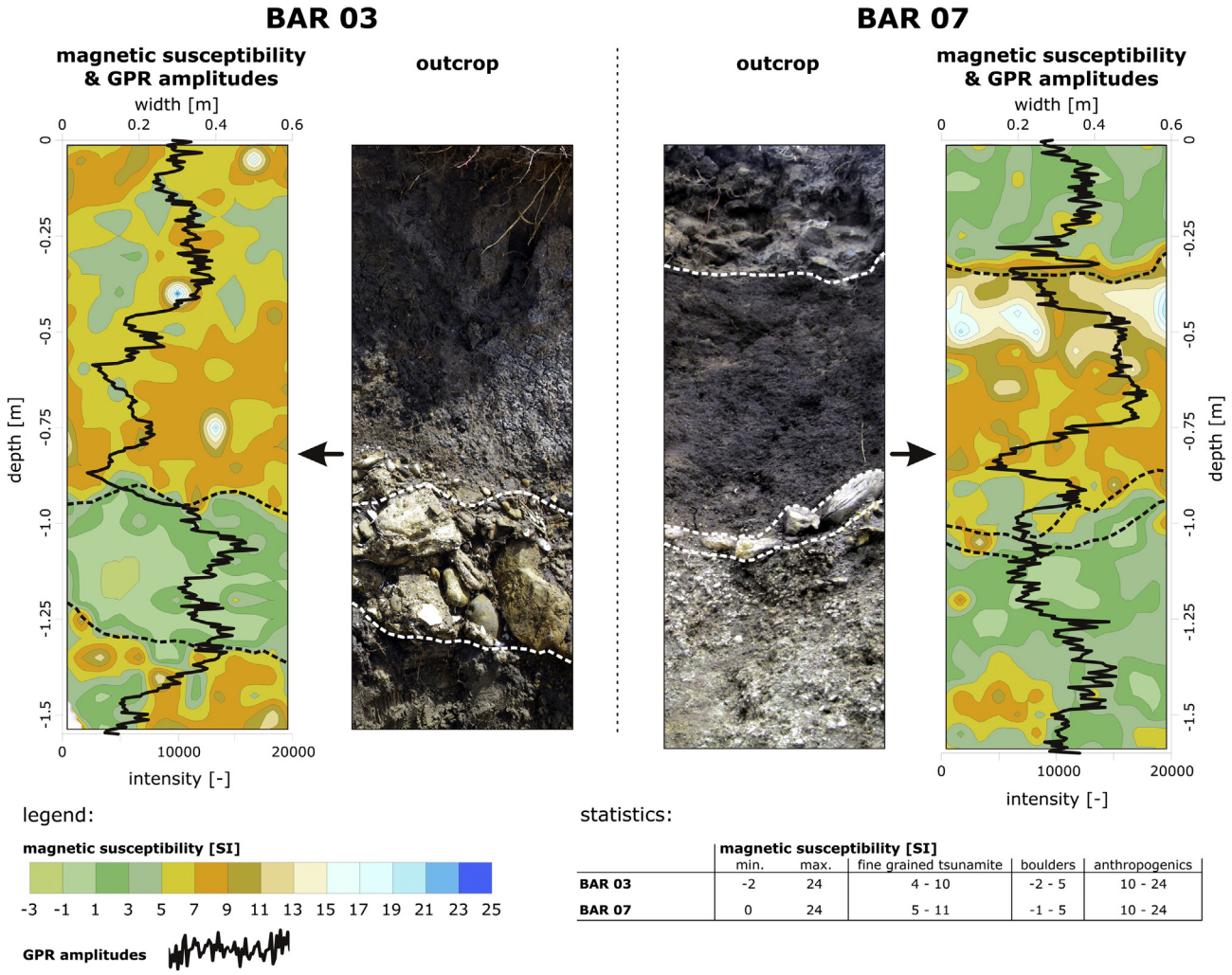

Fig. 7. Spatial magnetic susceptibility measurements and amplitude analysis of the outcrops BAR 03 (left) and BAR 07 (right) from 900 MHz antenna data. Amplitude data of the first 2 ns (equivalent ~8 cm) were used for each trace increment (2 cm). In the background of dimensionless amplitude curves are spatial magnetic susceptibility measurement data illustrated for the comparison of both methods. Legend and statistics of the measurements are shown at the bottom of the figure.

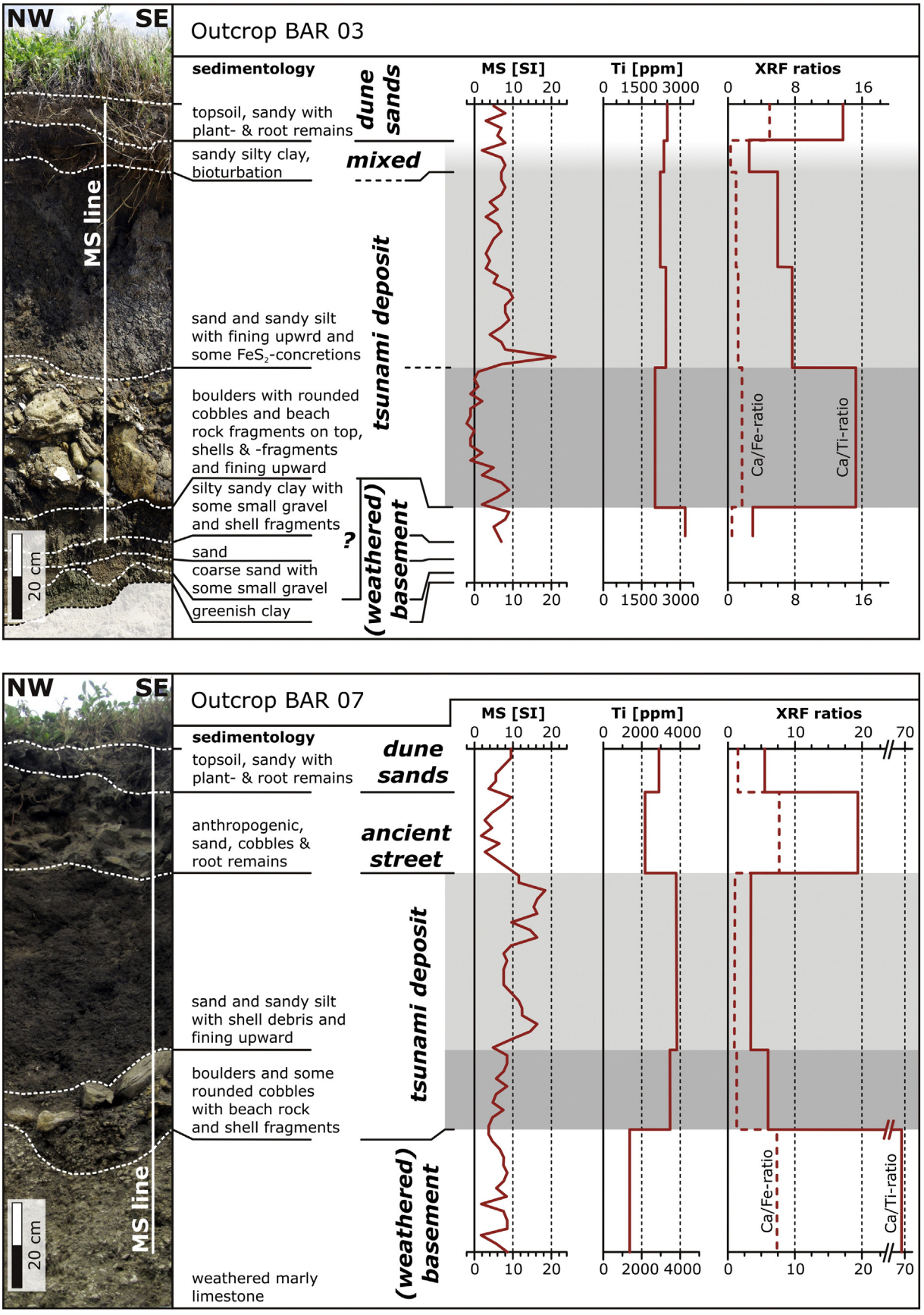

Fig. 8. Magnetic susceptibility (MS) line measurements compared to geochemical analysis of outcrop BAR 03 (top) and BAR 07 (B). All data of geochemical measurements are illustrated in a Supplementary Table.

there is also a change visible between the boulder and the dark coloured sand layer. The heterogeneous material above the coarse clast layers (e.g., at BAR 03, 0.2–1.1 m) has a changing elemental composition: both Ca/Fe- and Ca/Ti-ratios are lowering towards the top of the sandy deposit, while the amount of iron (Fe) or titanium (Ti) rises.

The XRF measurements can be used to support the results of the magnetic susceptibility measurements. This is due to the high amount of material composed of mineral rich components/elements, which is the cause of increasing magnetic susceptibility values in the anthropogenic or soil layers at the outcrops. Decreasing MS values in the sandy tsunami layers can be caused by higher concentrations of either organic or Ca-rich material. Furthermore, an increased amount of Ti was measured (Fig. 8, bottom) in the deposits below the ancient street remains at outcrop profile BAR 07, which possibly explains higher MS values in this area.

4.6. High resolution GPR profiles

GPR data using 900 MHz antenna reveal higher intensity values in areas consisting of coarse material, while areas with finer grained sediments have lower intensity values (Fig. 7). Only at outcrop BAR 07 (from −0.45 to −0.80 m below ancient street remains) excursions of higher intensity values were measured within the sandy tsunami deposit. The intensity values are plotted against MS results due to comparable results: the intensity curves behave quite similarly as the MS characteristics but with reversed values.

4.7. Spatial distribution characteristics of the tsunami deposits

A total of 144 GPR profiles were recorded on the beach cliff to study the internal architecture and spatial distribution of the tsunami deposit. Profiles were carried out parallel and perpendicular to the coastline to have closely spaced data (50 cm spacing) for dense GPR grid analysis.

The results of this study reveal channel structures and scours in the observed stratigraphy and GPR data (cf., Koster et al., 2013) as well as a wedging-out of the deposit (Fig. 9). In GPR profiles near outcrop BAR 03 the coarse grained layer with boulders and subangular stones is characterised by some hyperbolae reflection with v = 0.10–0.12 m/ns. The tsunami deposits (~0.2–1.2 m) have slight horizontal reflectors, while the layer boundaries are characterised by stronger (mostly) continuous reflectors. The basement material, as well some parts the (silty) sand layer of the tsunami deposit (~0.2–1.0 m), affects the radar waves with high attenuation.

Additionally, (pseudo-) 3D models of the layer boundaries have been calculated to evaluate further features (Fig. 10). These show that the lower boundary (~1.20 m) of the tsunami deposit dips with a mean value of ~6.2° towards the coast; having a standard deviation value of maximum 4.9° the calculated dipping angle varies from 1.1°–11.1° (see Table 4). Further features include possible mounds (Fig. 10A), ancient channels (Fig. 10B) and the (eroded) palaeo ground surface of the basement (Fig. 10C). A possible slope failure of the cliff (see Fig. 10B) was also detected due to an abrupt change in the deposit's basal depth.

A 3D layer model of the tsunami deposit's top and base in the vicinity of BAR 03 reveals further seaward-directed channel structures (Fig. 10, bottom). The tsunami deposit's top seems to be nearly flat.

The mean thickness of the deposits investigated with GPR is ~0.81 m, which corresponds with the sedimentological findings along the cliff. In the area around BAR 03 a minimum extent of the tsunami deposit (due to the limits of the measuring area) was detected up to ~20 m inland (from cliff), while the minimum extent at BAR 04 and BAR 06 (also due to the limits of the measuring area) is 12–13 m. The aspect of the base of the tsunami deposits is mainly seaward-directed, although the aspect's standard deviation is relatively high (Table 4).

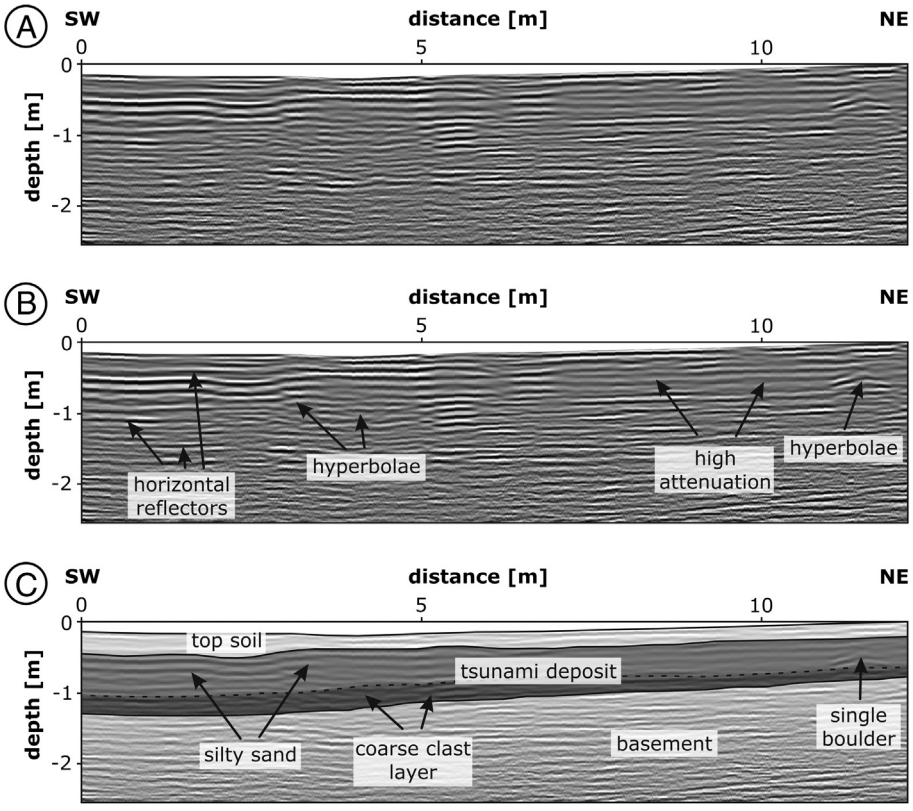

Fig. 9. GPR profile recorded perpendicular to the coastline close to outcrop BAR 03: (A) processed GPR profile, (B) processed and analysed GPR profile and (C) interpretation of the GPR profile.

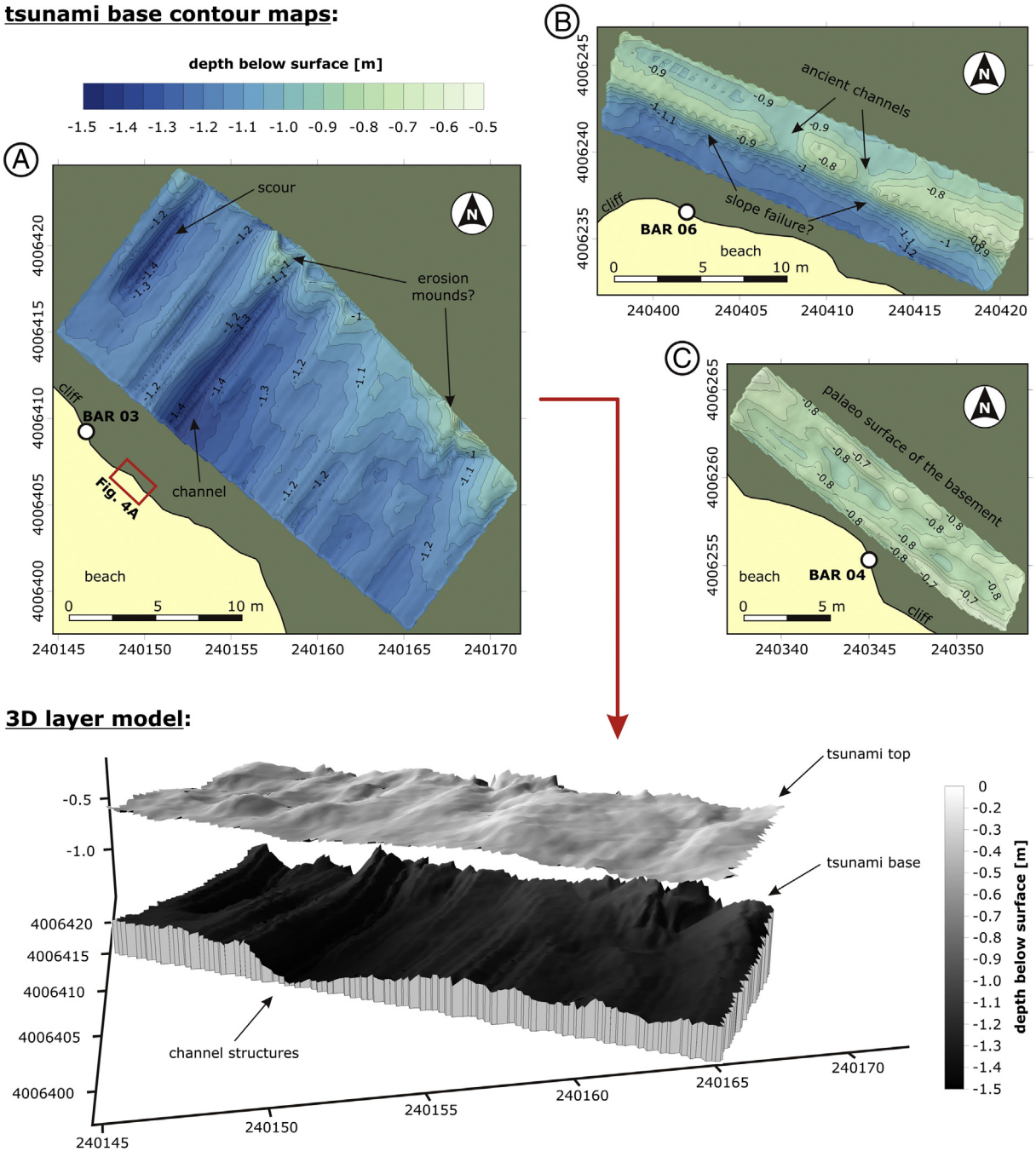

Fig. 10. Contour maps of pseudo-3D modelling of the picked GPR tsunami layers with erosional features close to outcrop (A) BAR 03 with location of Fig. 4A, (B) BAR 06 with possible slope failure parallel to the cliff and (C) BAR 04. (Pseudo-) 3D layer model below shows tsunami base and top characteristics of GPR investigations near outcrop BAR 03 (Fig. 10A). Parallel lines in a seaward direction may partially be artefacts from the input modelling data.

5. Discussion

5.1. Sedimentary characterisation

The sedimentological findings of this study comprise a coarse clast layer at the base of the tsunami deposit composed of a mixture of beachrock from marine Pleistocene terraces (MIS 5; Zazo et al., 1999) and Cretaceous/Eocene rocks, beach sand, gastropods, shells and shell fragments of a Pleistocene lowstand beach on the shelf. Furthermore, a subsequent overlying sand sheet is present which consists of marine beach sand, organic material from the marshlands, reworked pyrite concretions from the Mesozoic rocks as well as a mixture of reworked and recent marine foraminifera. Armoured mud balls are "floating" within the sand layer. This is most likely a backwash deposit because of the mixture of coastal and offshore sediments and seaward imbricated clasts inside the deposit. A debris flow origin of these deposits can be excluded due to the young marine components and the sedimentary features inside the deposit. Furthermore, a debris flow deposit would most likely have an inverse grading (e.g., Naylor, 1980; Takahashi, 2014). Formation and deposition of armoured mud balls during a debris flow can also be excluded due to the flow conditions being highly turbulent. The shear stress in such an event would be too high to keep such ball in one piece. Furthermore the concentration of suspension in a debris flow is too low compared to flow and transport conditions in a tsunami backwash.

Table 4
Parameters from the GPR pseudo-3D modelling with Surfer 11 software. The tsunami modelling includes the top, the base and the interlayer between the coarse cobbles/boulders and the fine grained upper part of the deposit. The thickness, dipping angle (slope) and aspect of the layers are calculated.

		3D GPR BAR 03			3D GPR BAR 04			3D GPR BAR 06		
		Top	Interlayer	Base	Top	Interlayer	Base	Top	Interlayer	Base
Depth	Min. [m]	−0.09 ± 0.05	−0.50 ± 0.05	−0.74 ± 0.05	0 ± 0.05	−0.33 ± 0.05	−0.59 ± 0.05	−0.01 ± 0.05	−0.51 ± 0.05	−0.65 ± 0.05
	max. [m]	−0.39 ± 0.05	−1.12 ± 0.05	−1.48 ± 0.05	−0.22 ± 0.05	−0.67 ± 0.05	−0.95 ± 0.05	−0.22 ± 0.05	−0.93 ± 0.05	−1.32 ± 0.05
	Mean [m]	−0.24 ± 0.05	−0.89 ± 0.05	−1.20 ± 0.05	−0.07 ± 0.05	−0.50 ± 0.05	−0.78 ± 0.05	−0.11 ± 0.05	−0.72 ± 0.05	−0.98 ± 0.05
	Standard deviation	0.05	0.10	0.11	0.04	0.04	0.06	0.05	0.13	0.18
Range	Mean [m]	0.65		0.31	0.43		0.28	0.51		0.26
			0.96			0.71			0.77	
Area	Mean [m^2]	335	324	323	77	74	74	144	144	142
Slope	Mean [°]	2.2	4.1	4.9	2.8	5.4	6.8	3.0	5.8	6.9
	Standard deviation	1.2	3.0	4.0	2.0	3.9	4.9	1.7	4.3	4.7
Aspect	Mean [°]	196.6	216.4	217.6	162.9	151.4	147.0	147.2	161.3	168.4
	Standard deviation		79.1	85.6	98.8	94.6	100.7	106.0	92.4	91.7

The thickness of the tsunami deposit along the cliff was investigated and compared with individual cliff heights and the altitude of the deposits at the corresponding locations (Fig. 4). The thickness of the tsunami deposit increases towards the middle part of the cliff and thins at the outer parts where the deposit was no longer detected. The cliff height does not exactly correlate with the thicknesses but there is a trend where the increasing cliff height contains a higher thickness of tsunami deposits. We interpret this as post-event erosional processes in a broad but shallow valley of the Barbate River northwards of the deposits. The spatial distribution of the deposit is limited along the cliff and is possibly influenced in western direction due to the occasional flooding of an ephemeral stream, which can result in regional erosion. Otherwise the thickness of the deposit along the cliff is relatively high compared to modern examples of tsunami deposits where preserved thicknesses exceeding 0.5 m are very rare (e.g., Morton et al., 2007; Kitamura et al., 2013). However, there are certain studies that report larger thicknesses of palaeotsunami deposits (e.g., Bruins et al., 2008; Hadler et al., 2013, 2014). Large thickness of the deposit is most likely due to wave backwash in a hemicycle/half moon bay shape (Fig. 1).

5.2. Bivariate plots of grain size statistics

The bivariate plots (Figs. 5, 6) indicate that the tsunami deposits from the study area plot in the field of a high-energy setting and are comparable to recent studies (e.g., Lario et al., 2002; Wassmer et al., 2010; Chagué-Goff et al., 2011; Szczuciński et al., 2012). The mean versus sorting diagram is well suited for this study for two reasons: firstly, it was applied by Lario et al. (2002) using samples from the same region (the Gulf of Cádiz) with a likely comparable setting, and secondly it includes characteristics for storm, fluviatile and tsunami deposits.

All samples from tsunami deposits cluster in the zone of fluvial and storm episodes/tsunamis. The reference samples from the marshlands plot in the low energy area of partially open to restricted estuary due to their flooded marshland character. The metric Steward's diagram uses a sorting vs. median plot (applied by Szczuciński et al. (2012) on tsunami deposits). Our samples are not distributed as the AD 2011 Tohoku-oki deposits, but do show similar characteristics (Fig. 5B). Moreover, the plotted reference samples indicate a mixture of both beach (marine) and marshland environments.

In the CM diagram all samples from the tsunami layer and the reference samples from the beach are located in high-energy depositional zones, whereas the marshland samples are located in low-energy zones (Fig. 6). The data plot is comparable to present studies on modern tsunami deposits (e.g., Wassmer et al., 2010; Chagué-Goff et al., 2011; Szczuciński et al., 2012) identifying tsunami deposits by their transport mechanism.

Three samples from the Tarifa region of Reicherter et al. (2010) show rolling deposition characteristics, which Cuven et al. (2013) attribute to deposits of the AD 1755 Lisbon tsunami. Regarding the CM diagram, the tsunami samples possibly represent a strong bottom current as tsunamis have very high velocities for run-up (10–20 m/s; Dawson and Stewart, 2007) and backwash flow (e.g., Bryant, 2008).

5.3. Micropalaeontology

The study of microfossils shows that the amount and number of species is relatively low. Most of the foraminifera in the beach reference samples and the tsunami deposit at the cliff are typical of a nearshore environment. *Elphidium crispum*, *Pullenia* sp. and *Ammonia beccarii* indicate a marine source of the dark coloured sandy (tsunami) deposit at the cliff. While *Globigerina* sp. and *Radiolaria* sp. are common in the Tertiary/Mesozoic rocks and, therefore, are reworked.

The marshland reference samples show an extended spectrum of species. Some of them (poorly preserved *Biticinella* sp., *Ticinella* sp., *Rotalipora* sp., *Heterohelix* sp. and *Glomospira* sp.) are reworked from

Cretaceous sediments from the hinterland (e.g., Grützner et al., 2012) and transported into the marshlands by the Barbate River.

During a tsunami event the transport of foraminifera can occur, which possibly results in reworked or broken specimens (e.g., Chaguéé-Goff et al., 2012). Post-tsunami processes within the deposits can lead to foraminifera breakage and dissolution, either partly or completely (e.g., Mamo et al., 2009; Yawsangratt et al., 2012). Hawkes et al. (2007) also reports the absence of very small species/foraminifera (such as it was found in the marshlands) within tsunami deposits.

5.4. Interpretation of MS in combination with high resolution GPR profiles

Higher values of MS can be explained by higher mineral content probably related to reworked Cretaceous ferromagnetic pyrite concretions within the deposits. The topsoil shows higher values than the values present in BAR03 due to anthropogenic influence or terrigenous input (e.g., clay minerals) and pedogenesis (e.g., Mullins, 1977). The topsoil MS has similar values to the underlying sandy silt/silty sand sequence. The soil as well as the first few centimetres of the sand layers are affected by root bioturbation and organic matter which modifies the mineral content. Another factor that increases the MS values is the migration of washed out elements/element compounds from anthropogenic material (here possibly: Ti) as it is present in the ancient street remains at outcrop BAR 07. The boulders at the base of the tsunami layer are dominated by diamagnetic materials such as shells, beachrock fragments and quartz/calcite pebbles, which cause low MS values.

In summary the tsunami deposit consists of silt, sand and boulder/gravel (from top to base) with an abrupt change of MS values at the boundary between sand/silty sand and gravel. The layer boundary between the tsunami deposit and the basement is characterised by a small change of MS values from 2 to 6.

The use of GPR profiles parallel to the outcrop walls was chosen to compare results with MS data, as homogenous magnetic mineral content of the deposit can affect both methods (MS: higher values; GPR: higher attenuation of electromagnetic waves). In areas of low MS values the GPR wave intensities are high and in areas of high MS values the GPR wave intensities are low. At outcrop BAR 07 the sandy tsunami deposit shows higher intensity values, because the sand contains reworked pyrite concretions (e.g., Daniels, 2004; Neal, 2004). XRD measurements for sediment mineralogy are recommended for future investigations.

5.5. Possible spatial distribution of the palaeotsunami deposit

3D modelling of the tsunami top and base from 2D-GPR data (Fig. 10) supports landward thinning/wedging out of the tsunami deposit, which is a common characteristic of tsunami deposits (e.g., Morton et al., 2007; Abe et al., 2012; Koster et al., 2014). Channels and scours (formed by tsunami or already existing) have also been observed by recent tsunami deposits (e.g., Matsumoto et al., 2010; Goto et al., 2014). The aspect data have high standard deviations, which are mainly due to complex geomorphological features at the base of the tsunami deposits; however, the main direction of seaward dipping is evidenced in the GPR data.

Based on the spatial distribution parameters and the recent findings, we reconstruct the former spatial distribution of the tsunami deposit. For such a model we considered the statistical parameters obtained from the GPR measurements with the sea level change within the last 4000 years (see Fig. 11).

The data presented here indicate a relatively thick deposit compared to modern examples of tsunami. The thickness of the tsunami deposits can be explained by the possible hemicycle/half moon bay shaped wave landfall and that the backwash would have been simultaneously blocked by the increased water level (Fig. 1). Cheng and Weiss (2013), Goto et al. (2014) and Sugawara et al. (2014) stated that a tsunami deposit's thickness, as well as the inundation depth, is controlled by several individual factors (e.g., morphology, offshore/onshore slope, available moveable sediment, backwash intensity) and is not only dependent of the power of tsunami landfall. The deposits are detectable in various places and not as a connected layer all over the coastal region, which is most likely due to post-event erosion (e.g., Szczuciński, 2012; Spiske et al., 2013).

5.6. Tsunami deposits related to a ~4000 BP event?

Dating of the tsunami deposits is challenging due to the reworking and transport of sediments from other places. Calibrated ages from the radiocarbon dating of shells within the tsunami deposit resulted in ages of >36,000 BP. This is critical due to two reasons: (1) yielded ages are at the detection limit of the ^{14}C-dating method, which is around 40,000 years and (2) if an age of >36,600 BP is accepted, then one also have to take into account that the sea level in this last glacial period was approx. 60 m lower than it is today (e.g., Siddall et al., 2003). The deposits represent reworked beach deposits. This would also imply a younger age for the tsunami event. The young age between 1260 and 1299 years BP comes from sample RC-BAR 04 (2A). This sample was taken at the interface with an overlying dune, which most likely does not relate to the tsunami event. Therefore, the investigated tsunami deposits at the cliff are attributed to tsunami occurrence before ~1300 years BP.

Combined data from the radiocarbon age of drill core DC 2 Zahara (see Reicherter et al., 2010) and the presented OSL datings from the tsunami deposits at the cliff indicate that the sediments (from the drill core Zahara DC 2) were deposited later than 5484 BP and a possible event age of ~4000 BP for the tsunami deposits in the cliff. It is still unclear whether the deposits at Zahara de los Atunes and Barbate belong to the same event, although the overall characteristics are similar.

If comparing the altitude of the deposit with the event age of ~4000 years and the mean uplift rates of 0.15 mm/year (e.g., Zazo et al., 1999) it becomes clear that the deposit was situated only 0.6 m

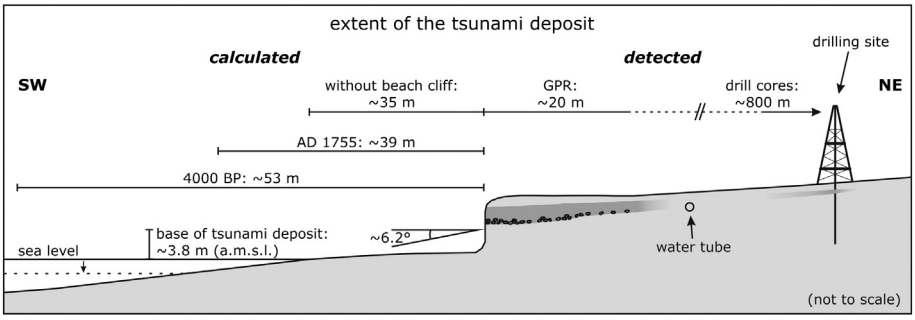

Fig. 11. Predicted original extent of the tsunami deposit using our results of recent tsunami deposit architecture, drilling results, and the sea level from 4000 BP when the tsunami event was triggered.

lower at time of deposition than at present and, therefore, was situated a few metres above mean sea and mean tide level.

The age dating fits well with the Holocene tsunami catalogue of Lario et al. (2011); two possible events are described between 4000 and 5000 BP. The younger event was evidenced by Ruiz et al. (2005). They found deposits from a 4200 BP tsunami event in the Doñana National Park at the Gulf of Cádiz. Baptista and Miranda (2009), Gràcia et al. (2010) and Lario et al. (2011) report that the older event took place around 5500–5000 BP. This event has to date not been detected along the coast between Conil and Algericas. According to the large error in the OSL dating method of ~1000 years it is suggested that both candidates could be the causative event or both events represent only 1 event due to error in dating.

The absence of older and younger tsunami deposits in the study area may underline this theory: geomorphologic, tectonic and erosion-related changes after successive (palaeo-) tsunami events along a highly variable coast possibly mix the signature of the events or even totally erode it. The tsunami deposits near Tarifa described by Reicherter et al. (2010) have not been dated up to now, but dating results from Cuven et al. (2013) from the same area indicate that the deposit belongs to the AD 1755 tsunami. Furthermore, Whelan and Kelletat (2005) describe medium to very coarse boulders at Cape Trafalgar close to Barbate beach attributed to the AD 1755 event.

6. Conclusions

It is most probable that remains of a ~4000 BP old tsunami deposit which affected the Atlantic coast of Andalucia have been discovered, as found in other places along the coast, and not the AD 1755 Lisbon tsunami as suggested in Reicherter et al. (2010).

This study reveals further details on the tsunami deposits in the vicinity of Barbate: the occurrence of clast coated mud balls with diameters between 0.4 m and 1.0 m. Beside an extended investigation on the sedimentology of several outcrops and reference samples, their grain size characteristics and bivariate plots, new features of palaeotsunami deposits are also presented from magnetic susceptibility and ground penetrating radar investigations.

Spatial magnetic susceptibility measurements can help to separate different horizons and identify the tsunami deposits from the surrounding sediments/soils. Combining this method with wave-reflection intensity from GPR on outcrop walls is a promising method. (Pseudo-) 3D subsurface models of the tsunami base and top by means of GPR data reveal geomorphological properties of the tsunami deposit.

In addition, this study shows that classical methods in palaeotsunami research, such as microforaminifera analysis and geochemical proxies, can be challenging and the outcome may be not significant as previously assumed. Only a combination of diverse methods using an advanced toolkit can provide evidence for high-energy deposits.

Acknowledgements

The first author is deeply grateful for being funded by RWTH Aachen Scholarships for Doctoral Students. We would like to thank the students Johannes Aichele, Alexander Rösner, Joschka Röth, Laura Roth, Fabian Stamm and Barbara Wolff for their efforts during fieldwork and in the laboratory. Very special thanks to Jack Mason concerning language correcting. Finally, we would like to thank both (anonymous) reviewers and Jasper Knight (editor in chief) for their constructive and helpful comments on our manuscript.

Appendix A. Supplementary data

Supplementary data to this article can be found online at http://dx.doi.org/10.1016/j.sedgeo.2014.09.006.

References

Abe, T., Goto, K., Sugawara, D., 2012. Relationship between the maximum extent of tsunami sand and the inundation limit of the 2011 Tohoku-oki tsunami on the Sendai Plain, Japan. Sediment. Geol. 282, 142–150.
Álvarez-Gómez, J.A., Aniel-Quiroga, Í., González, M., Otero, L., 2011. Tsunami hazard at the Western Mediterranean Spanish coast from seismic sources. Nat. Hazards Earth Syst. Sci. 11, 227–240.
Baptista, M.A., Miranda, J.M., 2009. Revision of the Portuguese catalog of tsunamis. Nat. Hazards Earth Syst. Sci. 9, 25–42.
Baptista, M.A., Miranda, P.M.A., Miranda, J.M., Victor, L., 1998. Constrains on the source of the 1755 Lisbon tsunami inferred from numerical modelling of historical data on the source of the 1755 Lisbon tsunami. J. Geodyn. 25, 159–174.
Baptista, M.A., Miranda, J.M., Omira, R., Antunes, C., 2011. Potential inundation of Lisbon downtown by a 1755-like tsunami. Nat. Hazards Earth Syst. Sci. 11, 3319–3326.
Baraza, J., Ercilla, G., Nelson, C.H., 1999. Potential geologic hazards on the eastern Gulf of Cadiz slope (SW Spain). Mar. Geol. 155, 191–215.
Birkmann, J., von Teichman, K., Welle, T., González, M., Olabarrieta, M., 2010. The unperceived risk to Europe's coasts: tsunamis and the vulnerability of Cadiz, Spain. Nat. Hazards Earth Syst. Sci. 10, 2659–2675.
Blott, S.J., Pye, K., 2001. GRADISTAT: a grain size distribution and statistics package for the analysis of unconsolidated sediments. Earth Surf. Process. Landf. 26, 1237–1248.
Brill, D., Klasen, N., Brückner, H., Jankaew, K., Scheffers, A., Kelletat, D., Scheffers, S., 2012. OSL dating of tsunami deposits from Phra Thong Island, Thailand. Quat. Geochronol. 10, 224–229.
Bronk Ramsey, C., 2009. Bayesian analysis of radiocarbon dates. Radiocarbon 51, 337–360.
Bruins, H.J., MacGillivray, J.A., Synolakis, C.E., Benjamini, C., Keller, J., Kisch, H.J., Klügel, A., van der Plicht, J., 2008. Geoarchaeological tsunami deposits at Palaikastro (Crete) and the Late Minoan IA eruption of Santorini. J. Archaeol. Sci. 35, 191–212.
Bryant, E., 2008. Tsunami — The Underrated Hazard. Springer, Praxis, Berlin, New York, Chichester, UK, p. 330 (Published in association with).
Chagué-Goff, C., 2010. Chemical signatures of palaeotsunamis: a forgotten proxy? Mar. Geol. 271, 67–71.
Chagué-Goff, C., Schneider, J.-L., Goff, J.R., Dominey-Howes, D., Strotz, L.C., 2011. Expanding the proxy toolkit to help identify past events — lessons from the 2004 Indian Ocean Tsunami and the 2009 South Pacific Tsunami. Earth Sci. Rev. 107, 107–122.
Chagué-Goff, C., Goff, J.R., Nichol, S., Dudley, W., Zawadzki, A., Bennett, J., Mooney, S., Fierro, D., Heijnis, H., Dominey-Howes, D., Courtney, C., 2012. Multi-proxy evidence for trans-Pacific tsunamis in the Hawai'ian Islands. Mar. Geol. 299–302, 77–89.
Cheng, W., Weiss, R., 2013. On sediment extent and runup of tsunami waves. Earth Planet. Sci. Lett. 362, 305–309.
Cuven, S., Paris, R., Falvard, S., Miot-Noirault, E., Benbakkar, M., Schneider, J.-L., Billy, I., 2013. High-resolution analysis of a tsunami deposit: case-study from the 1755 Lisbon tsunami in southwestern Spain. Mar. Geol. 337, 98–111.
Dabrio, C.J., Zazo, C., Goy, J.L., Sierro, F.J., Borja, F., Lario, J., González, J.A., Flores, J.A., 2000. Depositional history of estuarine infill during the last postglacial transgression (Gulf of Cadiz, Southern Spain). Mar. Geol. 162, 381–404.
Daniels, D.J., 2004. Ground penetrating radar. Institution of Electrical Engineers. Stevenage, p. 726.
Dawson, A.G., Stewart, I., 2007. Tsunami deposits in the geological record. Sediment. Geol. 200, 166–183.
Dawson, A.G., Hindson, R.A., Andrade, C., Freitas, C., Parish, R., Bateman, M., 1995. Tsunami sedimentation associated with the Lisbon earthquake of 1 November AD 1755: Boca do Rio, Algarve, Portugal. The Holocene 5, 209–215.
Dearing, J.A., 1994. Environmental magnetic susceptibility. Using the Bartington MS2 system. Kenilworth, p. 104, (Chi Pub).
Galbraith, R., Green, P., 1990. Estimating the component ages in a finite mixture. Nucl. Tracks Radiat. Meas. 17, 197–206.
Gjevik, B., Pedersen, G., Dybesland, E., Harbitz, C.B., Miranda, P.M.A., Baptista, M.A., Mendes-Victor, L., Heinrich, P., Roche, R., Guesmia, M., 1997. Modeling tsunamis from earthquake sources near Gorringe Bank southwest of Portugal. J. Geophys. Res. 102, 27931–27949.
Goto, K., Hashimoto, K., Sugawara, D., Yanagisawa, H., Abe, T., 2014. Spatial thickness variability of the 2011 Tohoku-oki tsunami deposits along the coastline of Sendai Bay. Mar. Geol. http://dx.doi.org/10.1016/j.margeo.2013.12.015 (in press).
Gracia, F.J., Alonso, C., Benavente, J., Anfuso, G., Del-Río, L., 2006. The different coastal records of the 1755 tsunami waves along the south Atlantic Spanish coast. Z. Geomorphol. Suppl. Vol. 146, 195–220.
Gràcia, E., Vizcaino, A., Escutia, C., Asioli, A., Rodés, Á., Pallàs, R., Garcia-Orellana, J., Lebreiro, S., Goldfinger, C., 2010. Holocene earthquake record offshore Portugal (SW Iberia): testing turbidite paleoseismology in a slow-convergence margin. Quat. Sci. Rev. 29, 1156–1172.
Grützner, C., Reicherter, K., Hübscher, C., Silva, P.G., 2012. Active faulting and neotectonics in the Baelo Claudia area, Campo de Gibraltar (southern Spain). Tectonophysics 554–557, 127–142.
Gutscher, M.-A., Malod, J., Rehault, J.-P., Contrucci, I., Klingelhoefer, F., Mendes-Victor, L., Spakman, W., 2002. Evidence for active subduction beneath Gibraltar. Geology 30, 1071–1074.
Gutscher, M.-A., Baptista, M.A., Miranda, J.M., 2006. The Gibraltar Arc seismogenic zone (part 2): constraints on a shallow east dipping fault plane source for the 1755 Lisbon earthquake provided by tsunami modeling and seismic intensity. Tectonophysics 426, 153–166.
Gutscher, M.-A., Dominguez, S., Westbrook, G.K., Leroy, P., 2009. Deep structure, recent deformation and analog modeling of the Gulf of Cadiz accretionary wedge: implications for the 1755 Lisbon earthquake. Tectonophysics 475, 85–97.

Hadler, H., Vött, A., Koster, B., Mathes-Schmidt, M., Mattern, T., Ntageretzis, K., Reicherter, K., Willershäuser, T., 2013. Multiple late-Holocene tsunami landfall in the eastern Gulf of Corinth recorded in the palaeotsunami geo-archive at Lechaion, harbour of ancient Corinth (Peloponnese, Greece). Z. Geomorphol. Suppl. Issue 57, 139–180.

Hadler, H., Baika, K., Pakkanen, J., Fischer, P., Henning, P., Ntageretzis, P., Röbke, B., Willershäuser, T., Vött, A., 2014. Palaeotsunami impact on the ancient harbour site of Kyllini (western Peloponnese, Greece) based on a multi-proxy approach. Z. Geomorphol. Suppl. Issue (in press).

Hawkes, A.D., Bird, M., Cowie, S., Grundy-Warr, C., Horton, B.P., Shau Hwai, A.T., Law, L., Macgregor, C., Nott, J., Ong, J.E., Rigg, J., Robinson, R., Tan-Mullins, M., Sa, T.T., Yasin, Z., Aik, L.W., 2007. Sediments deposited by the 2004 Indian Ocean Tsunami along the Malaysia–Thailand Peninsula. Marine Geology 242, 169–190.

Hindson, R.A., Andrade, C., Dawson, A.G., 1996. Sedimentary processes associated with the tsunami generated by the 1755 Lisbon earthquake on the Algarve coast, Portugal. Phys. Chem. Earth 21, 57–63.

Hofrichter, R., 2003. Das Mittelmeer - Fauna, Flora, Ökologie. Band II/1: Bestimmungsführer. Verlag, Heidelberg, p. 859 (Spektrum, Akad).

Kaabouben, F., Baptista, M.A., Iben Brahim, A., El Mouraouah, A., Toto, A., 2009. On the moroccan tsunami catalogue. Nat. Hazards Earth Syst. Sci. 9, 1227–1236.

Kitamura, A., Fujiwara, O., Shinohara, K., Akaike, S., Masuda, T., Ogura, K., Urano, Y., Kobayashi, K., Tamaki, C., Mori, H., 2013. Identifying possible tsunami deposits on the Shizuoka Plain, Japan and their correlation with earthquake activity over the past 4000 years. The Holocene 23, 1684–1698.

Kortekaas, S., Dawson, A.G., 2007. Distinguishing tsunami and storm deposits: an example from Martinhal, SW Portugal. Sediment. Geol. 200, 208–221.

Koster, B., Hadler, H., Vött, A., Reicherter, K., 2013. Application of GPR for visualising spatial distribution and internal structures of tsunami deposits — case studies from Spain and Greece. Z. Geomorphol. Suppl. Issue 57, 29–45.

Koster, B., Hoffmann, G., Grützner, C., Reicherter, K., 2014. Ground penetrating radar facies of inferred tsunami deposits on the shores of the Arabian Sea (Northern Indian Ocean). Mar. Geol. 351, 13–24.

Lario, J., Spencer, C., Plater, A., Zazo, C., Goy, J., Dabrio, C., 2002. Particle size characterisation of Holocene back-barrier sequences from North Atlantic coasts (SW Spain and SE England). Geomorphology 42, 25–42.

Lario, J., Zazo, C., Goy, J.L., Silva, P.G., Bardají, T., Cabero, A., Dabrio, C., 2011. Holocene palaeotsunami catalogue of SW Iberia. Quat. Int. 242, 196–200.

Loeblich, A.R., Tappan, H., 1988. Foraminiferal Genera and Their Classification. Van Nostrand Reinhold, New York, p. 2114.

Luque, L., Lario, J., Zazo, C., Goy, J.L., Dabrio, C.J., Silva, P.G., 2001. Tsunami deposits as paleoseismic indicators: examples from the Spanish coast. Acta Geol. Hisp. 36, 197–211.

Luque, L., Lario, J., Civis, J., Silva, P.G., Zazo, C., Goy, J.L., Dabrio, C.J., 2002. Sedimentary record of a tsunami during Roman times, Bay of Cadiz, Spain. J. Quat. Sci. 17, 623–631.

Mamo, B., Strotz, L.C., Dominey-Howes, D., 2009. Tsunami sediments and their foraminiferal assemblages. Earth Sci. Rev. 96, 263–278.

Matias, L.M., Cunha, T., Annunziato, A., Baptista, M.A., Carrilho, F., 2013. Tsunamigenic earthquakes in the Gulf of Cadiz: fault model and recurrence. Nat. Hazards Earth Syst. Sci. 13, 1–13.

Matsumoto, D., Shimamoto, T., Hirose, T., Gunatilake, J., Wickramasooriya, A., DeLile, J., Young, S., Rathnayake, C., Ranasooriya, J., Murayama, M., 2010. Thickness and grain-size distribution of the 2004 Indian Ocean tsunami deposits in Periya Kalapuwa Lagoon, eastern Sri Lanka. Sediment. Geol. 230, 95–104.

Mendes-Victor, L.A., Ansal, A., Azevedo, J., Oliveira, C.S., Ribeiro, A., 2009. The 1755 Lisbon Earthquake: Revisited. Springer Netherlands, Dordrecht, p. 597.

Morales, J., Borrego, J., San Miguel, E., López-González, N., Carro, B., 2008. Sedimentary record of recent tsunamis in the Huelva Estuary (southwestern Spain). Quat. Sci. Rev. 27, 734–746.

Moreno, I.M., Ávila, A., Losada, M.Á., 2010. Morphodynamics of intermittent coastal lagoons in Southern Spain: Zahara de los Atunes. Geomorphology 121, 305–316.

Morton, R.A., Gelfenbaum, G., Jaffe, B.E., 2007. Physical criteria for distinguishing sandy tsunami and storm deposits using modern examples. Sediment. Geol. 200, 184–207.

Mulder, T., Gonthier, E., Lecroart, P., Hanquiez, V., Marches, E., Voisset, M., 2009. Sediment failures and flows in the Gulf of Cadiz (eastern Atlantic). Mar. Pet. Geol. 26, 660–672.

Mullins, C.E., 1977. Magnetic susceptibility of the soil and its significance in soil science — a review. J. Soil Sci. 28, 223–246.

Murray, J.W., 2008. Ecology and Applications of Benthic Foraminifera. Cambridge University Press, Cambridge, p. 440.

Murray, A., Wintle, A., 2000. Luminescence dating of quartz using an improved single-aliquot regenerative-dose protocol. Radiat. Meas. 32, 57–73.

Naylor, M.A., 1980. The origin of inverse grading in muddy debris flow deposits—a review. J. Sediment. Petrol. 50, 1111–1116.

Neal, A., 2004. Ground-penetrating radar and its use in sedimentology: principles, problems and progress. Earth Sci. Rev. 66, 261–330.

Reicherter, K.R., Vonberg, D., Koster, B., Fernández-Steeger, T., Grützner, C., Mathes-Schmidt, M., 2010. The sedimentary inventory of tsunamis along the southern Gulf of Cádiz (southwestern Spain). Z. Geomorphol. Suppl. Issue 54, 147–173.

Reimer, P.J., Bard, E., Bayliss, A., Beck, J., Blackwell, P.G., Bronk Ramsey, C., Buck, C.E., Cheng, H., Edwards, R.L., Friedrich, M., Grootes, P.M., Guilderson, T.P., Haflidason, H., Hajdas, I., Hatté, C., Heaton, T.J., Hoffmann, D.L., Hogg, A.G., Hughen, K.A., Kaiser, K.F., Kromer, B., Manning, S.W., Niu, M., Reimer, R.W., Richards, D.A., Scott, E.M., Southon, J.R., Staff, R.A., Turney, C.S.M., van der Plicht, J., 2013. IntCal13 and Marine13 Radiocarbon Age Calibration Curves 0–50,000 Years cal BP. Radiocarbon 55, 1869–1887.

Rodríguez-Vidal, J., Cáceres, L.M., Abad, M., Ruiz, F., González-Regalado, M.L., Finlayson, C., Finlayson, G., Fa, D., Rodríguez-Llanes, J.M., Bailey, G., 2011a. The recorded evidence of AD 1755 Atlantic tsunami on the Gibraltar coast. J. Iber. Geol. 37, 177–193.

Rodríguez-Vidal, J., Ruiz, F., Cáceres, L.M., Abad, M., González-Regalado, M.L., Pozo, M., Carretero, M.I., Monge Soares, A.M., Toscano, F.G., 2011b. Geomarkers of the 218–209 BC Atlantic tsunami in the Roman Lacus Ligustinus (SW Spain): a palaeogeographical approach. Quat. Int. 242, 201–212.

Ruiz, F., Rodríguez-Ramírez, A., Cáceres, L.M., Vidal, J.R., Carretero, M.I., Abad, M., Olías, M., Pozo, M., 2005. Evidence of high-energy events in the geological record: mid-Holocene evolution of the southwestern Doñana National Park (SW Spain). Palaeogeogr. Palaeoclimatol. Palaeoecol. 229, 212–229.

Ruiz, F., Abad, M., Rodríguez-Vidal, J., Cáceres, L.M., González-Regalado, M.L., Carretero, M.I., Pozo, M., Toscano, F.G., 2008. The geological record of the oldest historical tsunamis in southwestern Spain. Riv. Ital. Paleontol. Stratigr. 114, 145–154.

Ruiz, F., Rodríguez-Vidal, J., Abad, M., Cáceres, L.M., Carretero, M.I., Pozo, M., Rodríguez-Llanes, J.M., Gómez-Toscano, F., Izquierdo, T., Font, E., Toscano, A., 2013. Sedimentological and geomorphological imprints of Holocene tsunamis in southwestern Spain: an approach to establish the recurrence period. Geomorphology 203, 97–104.

Schiebel, R., Hemleben, C., 2005. Modern planktic foraminifera. Paläontol. Z. 79, 135–148.

Siddall, M., Rohling, E.J., Almogi-Labin, A., Hemleben, C., Meischner, D., Schmelzer, I., Smeed, D.A., 2003. Sea-level fluctuations during the last glacial cycle. Nature 423, 853–858.

Soloviev, S.L., 1990. Tsunamigenic zones in the Mediterranean Sea. Nat. Hazards 3, 183–202.

Spiske, M., Piepenbreier, J., Benavente, C., Bahlburg, H., 2013. Preservation potential of tsunami deposits on arid siliciclastic coasts. Earth Sci. Rev. 126, 58–73.

Sugawara, D., Goto, K., Jaffe, B.E., 2014. Numerical models of tsunami sediment transport — current understanding and future directions. Mar. Geol. 352, 295–320.

Szczuciński, W., 2012. The post-depositional changes of the onshore 2004 tsunami deposits on the Andaman Sea coast of Thailand. Nat. Hazards 60, 115–133.

Szczuciński, W., Kokociński, M., Rzeszewski, M., Chagué-Goff, C., Cachão, M., Goto, K., Sugawara, D., 2012. Sediment sources and sedimentation processes of 2011 Tohoku-oki tsunami deposits on the Sendai Plain, Japan — insights from diatoms, nannoliths and grain size distribution. Sediment. Geol. 282, 40–56.

Takahashi, T., 2014. Debris Flow: Mechanics, Prediction, and Countermeasures, 2nd ed. Taylor and Francis, Hoboken, p. 551.

Vött, A., Bareth, G., Brückner, H., Lang, F., Sakellariou, D., Hadler, H., Ntageretzis, K., Willershäuser, T., 2011. Olympia's Harbour Site Pheia (Elis, Western Peloponnese, Greece) Destroyed by Tsunami Impact. Die Erde 142, 259–288.

Wassmer, P., Schneider, J.-L., Fonfrège, A.-V., Lavigne, F., Paris, R., Gomez, C., 2010. Use of anisotropy of magnetic susceptibility (AMS) in the study of tsunami deposits: application to the 2004 deposits on the eastern coast of Banda Aceh, North Sumatra, Indonesia. Mar. Geol. 275, 255–272.

Whelan, F., Kelletat, D., 2005. Boulder deposits on the southern Spanish Atlantic coast: possible evidence for the 1755 ad Lisbon tsunami? Sci. Tsunami Hazards 23, 25–38.

Yawsangratt, S., Szczuciński, W., Chaimanee, N., Chatprasert, S., Majewski, W., Lorenc, S., 2012. Evidence of probable paleotsunami deposits on Kho Khao Island, Phang Nga Province, Thailand. Nat. Hazards 63, 151–163.

Zazo, C., Silva, P.G., Goy, J.L., Hillaire-Marcel, C., Ghaleb, B., Lario, J., Bardají, T., González, A., 1999. Coastal uplift in continental collision plate boundaries: data from the Last Interglacial marine terraces of the Gibraltar Strait area (south Spain). Tectonophysics 301, 95–109.